MATERIALS SCIENCE

Ultrahigh sensitivity of methylammonium lead tribromide perovskite single crystals to environmental gases

Hong-Hua Fang,[1] Sampson Adjokatse,[1] Haotong Wei,[2] Jie Yang,[1] Graeme R. Blake,[1] Jinsong Huang,[2] Jacky Even,[3] Maria Antonietta Loi[1]*

One of the limiting factors to high device performance in photovoltaics is the presence of surface traps. Hence, the understanding and control of carrier recombination at the surface of organic-inorganic hybrid perovskite is critical for the design and optimization of devices with this material as the active layer. We demonstrate that the surface recombination rate (or surface trap state density) in methylammonium lead tribromide (MAPbBr$_3$) single crystals can be fully and reversibly controlled by the physisorption of oxygen and water molecules, leading to a modulation of the photoluminescence intensity by over two orders of magnitude. We report an unusually low surface recombination velocity of 4 cm/s (corresponding to a surface trap state density of 10^8 cm^{-2}) in this material, which is the lowest value ever reported for hybrid perovskites. In addition, a consistent modulation of the transport properties in single crystal devices is evidenced. Our findings highlight the importance of environmental conditions on the investigation and fabrication of high-quality, perovskite-based devices and offer a new potential application of these materials to detect oxygen and water vapor.

INTRODUCTION

Hybrid perovskites have led to a whole new generation of solar devices with remarkable power conversion efficiency over 22% (1–5). This impressive performance in solar cells has also spawned the exploration of diverse applications from light-emitting diodes (6) and lasers (7, 8) to photodetectors (9, 10), etc. Perovskites have been shown to have superior optoelectronic properties, such as a tunable direct bandgap, high absorption coefficient, and balanced electron and hole transport (11–13). Similar to other more traditional semiconductors, the stability and performance of hybrid perovskite devices are strongly dependent on the defect states and the film morphology, which have a great effect on the carrier lifetime (14–17). Great effort has been devoted to produce large-grained perovskite films, improving their crystalline quality (18–20). In single crystals of methylammonium lead triiodide (MAPbI$_3$) and methylammonium lead tribromide (MAPbBr$_3$), carrier diffusion lengths over 100 μm and bulk trap state densities of the order of 10^9 to 10^{10} per cubic centimeter have been demonstrated (21, 22). Surface recombination represents an important loss of carriers and often plays a decisive role in determining the optoelectronic properties of semiconductors, where interfaces between different materials are crucial for the device to function. A low surface recombination rate is required to try to approach the thermodynamic efficiency limits for solar cells and devise other efficient optoelectronic devices. Thus, understanding and controlling the recombination of carriers at the surface of perovskite crystals is critically important for designing and optimizing devices.

Recently, a number of studies have shown that the interaction between hybrid perovskite materials and their environment has a significant impact not only on the perovskite morphology or photostability but also on the optoelectronic properties (23–26). For instance, Grancini and co-workers (27) reported that moisture and possibly oxygen

molecules can cause perovskite lattice strain and a shift in the photoluminescence (PL) spectrum. Tian and co-workers (25) showed a PL yield enhancement in oxygen, which is attributed to a photochemical reaction located both at the surface and in the bulk of MAPbI$_3$. Similarly, Müller et al. (26) found that water infiltration into MAPbI$_3$ films increases its ionic conductivity. However, the interaction mechanism is only partially known and remains controversial. In polycrystalline thin films, the intrinsic response of the optoelectronic properties to the environment may be shielded by the microstructure quality and noncrystalline domains. On the other hand, grain boundaries and noncrystalline domains are absent in single crystals, making them the ideal platform to probe the intrinsic material properties as well as the surface recombination, and hence providing insight into the limitations in improving perovskite polycrystalline thin film solar cells.

Here, we investigate the optical properties of MAPbBr$_3$ single crystals by single- and two-photon excitation, and we demonstrate an unusually low surface recombination velocity (SRV) of 4 cm/s in these crystals, which can be modulated by the physisorption of O$_2$ and H$_2$O molecules. Thus, we reveal that the photophysical properties of MAPbBr$_3$ single crystals are ultrasensitive to their environment. Moreover, the tunability of the photophysical and charge transport properties of the MAPbBr$_3$ single crystals is fully and quantitatively reversible. This phenomenon could therefore be at the basis for the development of sensitive MAPbBr$_3$-based gas detectors.

RESULTS AND DISCUSSION

PL modulation effect on crystals

The MAPbBr$_3$ single crystals were prepared from solution by inverse temperature crystallization (ITC) and antisolvent vapor-assisted crystallization (AVC) methods. The inset of Fig. 1A shows an image of an MAPbBr$_3$ single crystal with dimensions of ~5 × 3 × 1.7 mm^3 grown by the ITC method. The crystal adopts the cubic $Pm\bar{3}m$ space group at

[1]Zernike Institute for Advanced Materials, University of Groningen, Nijenborgh 4, 9747 AG Groningen, Netherlands. [2]Department of Mechanical and Materials Engineering, University of Nebraska–Lincoln, Lincoln, NE 68588, USA. [3]Université Européenne de Bretagne, INSA, FOTON, UMR 6082, 35708 Rennes, France.
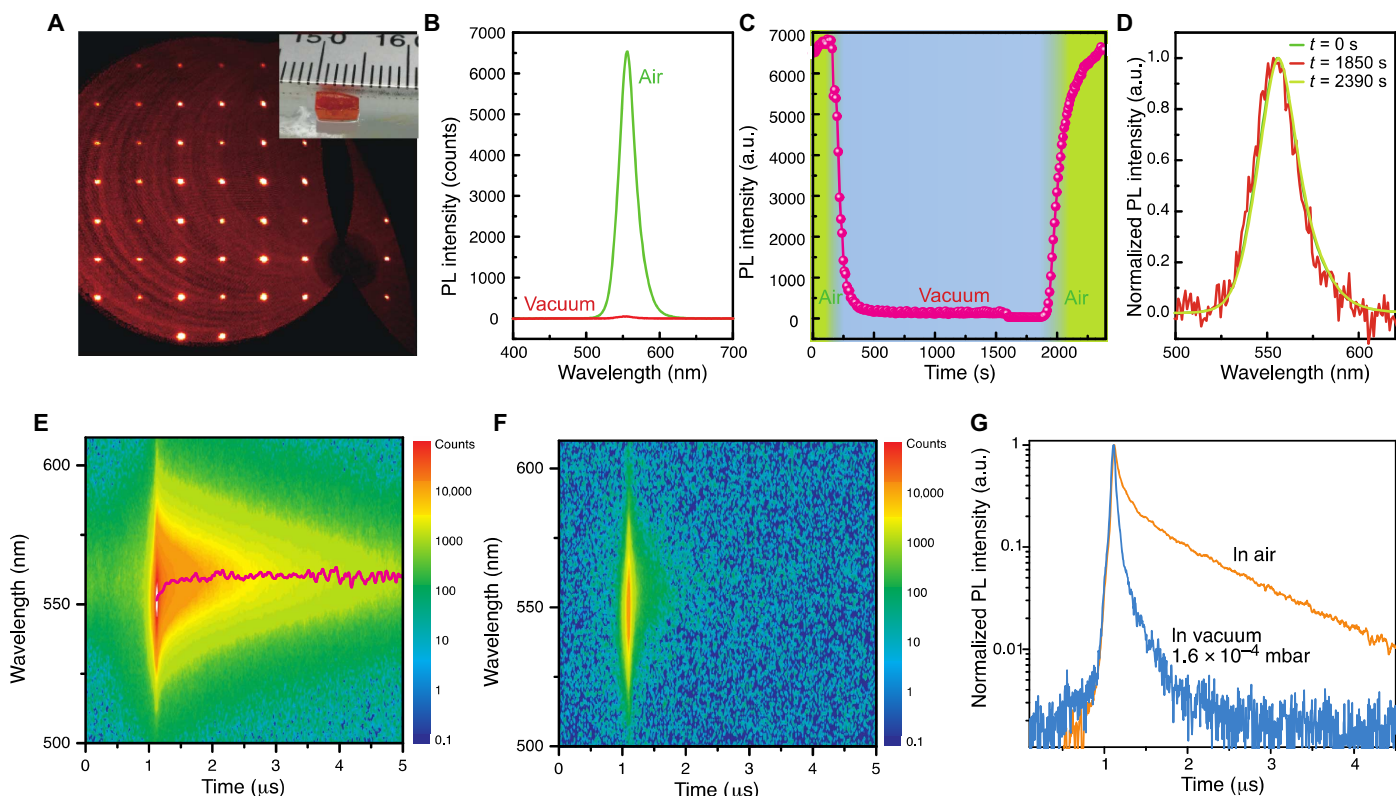*Corresponding author. Email: m.a.loi@rug.nl

Fig. 1. XRD and optical properties of MAPbBr$_3$ single crystals. (**A**) *hk0* reciprocal lattice plane reconstructed from MAPbBr$_3$ single crystal XRD data at room temperature. Inset: Image of one of the measured crystals grown from solution. (**B**) PL spectra in vacuum and air (the PL intensity in vacuum is two orders of magnitude lower than in air). (**C**) Variation in PL intensity of MAPbBr$_3$ crystals from air-vacuum-air environments. a.u., arbitrary units. (**D**) Normalized PL spectra at different times in (C). (**E** and **F**) Two-dimensional (2D) pseudocolor plots of TRPL spectra taken in air and vacuum with an excitation power density of 0.71 μJ/cm^2. (**G**) Decay of the PL at a wavelength of 560 nm in air and vacuum.

room temperature. Figure 1A presents the *hk0* reciprocal lattice plane reconstructed from raw single crystal x-ray diffraction (XRD) data collected at 295 K. The sharp spots show the high quality of the crystals. A powder diffraction pattern was collected at room temperature (see fig. S1) with peaks at 14.92°, 21.11°, 30.07°, 33.71°, 37.11°, 43.05°, and 45.77°. Conversion of the peak positions to interplanar spacings shows that these peaks correspond to the (100), (110), (200), (210), (211), (220), and (300) planes, respectively.

Under ambient conditions, the excitation of the crystal with a 400-nm wavelength femtosecond laser (75-MHz repetition rate) results in strong yellow-green fluorescence. The corresponding emission peak is located at 556 nm (Fig. 1B) near the absorption onset (2.23 eV), as is revealed by the PL excitation spectrum (see fig. S2). The crystals show superior photostability under the same ambient conditions; the PL intensity remained constant even after more than 3.5 hours of continuous optical pumping (see fig. S3). However, we found that the PL intensity of the MAPbBr$_3$ crystal can be modulated when the crystals are exposed to different environments. For instance, when the atmospheric pressure is changed, the PL intensity also changes instantaneously. The PL intensity is reduced by more than two orders of magnitude when the sample chamber is evacuated from atmospheric pressure to 1.3×10^{-4} mbar, as shown in Fig. 1B. The correlation between the emission intensity and the controlled pressure is clearly seen when the gas pressure is further reduced to 10^{-4} mbar (see fig. S4). It is noticeable that the PL intensity

reverts to its original magnitude when the chamber is refilled with air to ambient pressure, clearly showing the reversibility of these "deactivation" and "activation" processes.

Figure 1C shows the reversible variation of the PL intensity on the chamber pressure. The PL intensity decreases to 10% within 120 s (160 to 280 s) when the chamber is evacuated. It further decreases slowly to 0.4% of the initial intensity in air after about 1750 s in vacuum. The observed PL modulation effect in the crystals is very high, and thus macroscopically visible (see movie S1). Figure 1D shows the normalized PL spectra corresponding to various times in the PL intensity plot in Fig. 1C, where it is obvious that the PL in vacuum is only slightly blueshifted compared with that in air. The increased surface recombination in vacuum leads to a lower fraction of the photogenerated carriers to diffuse toward the interior of the crystal, and therefore in this case, the PL is less affected by reabsorption. We note that the PL modulation effect is observed in both crystals prepared by ITC (Fig. 1) and AVC methods (see fig. S5), as well as in crystals cleaved inside an N$_2$-filled glove box (see fig. S6).

To understand how the presence of air affects the PL, we investigated the dynamics of photoexcitation in the MAPbBr$_3$ single crystals in different environments (Fig. 1, E and F). With an excitation power density of 0.71 μJ/cm^2 (400-nm wavelength), the decay time of the crystal measured in air shows an initial fast component with a lifetime of ≈59 ns (77.2%) and a slower component with a lifetime of ≈818 ns (22.8%) (Fig. 1G). The underlying mechanism for the extremely long carrier lifetime in the

hybrid perovskites is not fully understood. Recently, Rashba spin-orbit coupling has been proposed as one of the possible explanations (28).

In vacuum, the PL lifetime of the MAPbBr$_3$ single crystals is much shorter (Fig. 1G), and its determination is limited by the instrumental resolution in the configuration used to measure the crystal in air. A lifetime of 22 ns is measured using a shorter time window (see fig. S7). Similar to our observations for steady-state PL, the time-resolved PL (TRPL) reverts to its initial behavior a few minutes after the chamber is refilled with air. This ability to "reset" the darkening as an effect of air exposure suggests that the gas molecules are physisorbed rather than chemisorbed on the crystal surface.

Physisorption of gas molecules

To determine which gas molecules are responsible for the observed optical behavior and to assess the influence of atmospheric gas adsorption on the crystal surface, the PL intensity variation was monitored in different gas environments. Optical spectroscopic measurements were performed in the following atmospheres: moist air, dry N$_2$, He, CO$_2$, a mixture of O$_2$ (20%) and He (80%), moist N$_2$, moist O$_2$, and vacuum. Before each gas exposure and measurement, the sample chamber containing the crystal was evacuated to a pressure from 10^{-4} to 10^{-5} mbar and left in vacuum for about 30 min before filling the chamber with the test gas. In the case of the measurements performed in vacuum, the crystal with the 400-nm excitation laser beam incident was left in the chamber for an additional 30 min. In each of the measurements, the laser with a pulse repetition rate of 1.4 MHz was kept at a constant fluence of 0.71 μJ/cm^2. The PL of the sample was monitored every 10 s.

The PL intensity variation as a function of time for the single crystal under illumination in different gas atmospheres is shown in Fig. 2. Exposure of the crystal to dry N$_2$, CO$_2$, or Ar (Fig. 2A) has no influence on the PL intensity. However, the PL intensity increases rapidly in the presence of air, dry O$_2$, and moist N$_2$, as shown in Fig. 2B. It is worth noting that the most rapid and intense PL enhancement is observed in the air-exposed crystal, whereas the PL intensity recovers much more slowly in dry O$_2$ and moist N$_2$. These data clearly indicate that the PL enhancement is due to the molecular property of O$_2$ and H$_2$O. Moreover, the presence of a combination of oxygen and water molecules further promotes the activation process to a level that is very similar to that observed in air (see fig. S8). All these intensity variations in different gases occur with essentially no difference in the wavelength and shape of the emission peak (a spread of about 5 nm in the peak wavelength can be seen in the normalized PL spectrum reported in fig. S9). The measurements reported here are highly reproducible and independent of the sample history. Thus, the effect of gas exposure can be reset when the chamber is evacuated. This also implies that the interaction between the defect sites and the gas molecules is weak (they are physisorbed), but it dictates the optical emission of the material.

Bulk and surface optical properties of single crystals

The results reported in the previous section demonstrate that O$_2$ and H$_2$O molecules passivate the charge traps in MAPbBr$_3$ single crystals. However, it is unclear where the traps are located, whether at the crystal surface or in the bulk of the crystal. To selectively probe the bulk properties of our crystals, an 800-nm femtosecond laser was used to excite the crystal with photon energy below the bandgap energy. Figure 3A shows the TRPL under excitation of the 800-nm femtosecond laser with a photocarrier density of around 1.9×10^{13} cm^{-3}. Under two-photon excitation, the laser can penetrate deep into the bulk and excite the interior region

of the crystal (see inset of Fig. 3B). Therefore, the bulk properties can be measured in this way, neglecting the contributions from the surface (29). The steady-state emission peak wavelength is slightly redshifted (566 nm) compared to the emission when the crystal is excited with the 400-nm laser (556 nm). The lifetimes extracted from the TRPL curves are $t_1 = 34$ ns and $t_2 = 4.5$ μs, as shown in Fig. 3B. Figure 3C shows the two-photon excited PL spectra in vacuum and ambient air. Unlike in the 400-nm laser excitation experiment, the PL intensity difference is much smaller under two-photon excitation. The PL intensity variation under two-photon excitation is within the uncertainty of the measurement (fig. S10). The fact that the optical properties of the bulk of the crystal are less affected by O$_2$ and H$_2$O molecules allows us to conclude that most of the trap states passivated by O$_2$ and H$_2$O are localized near the MAPbBr$_3$ crystal surface.

Under the single-photon excitation, the penetration depth of the laser in the crystal is only ~150 nm (30). Thus, only optical properties in the near-surface region up to the penetration depth are probed. Therefore, the photocarrier recombination is observed to be strongly affected by the surface properties. Figure 3D shows a 2D pseudocolor plot of the TRPL of a freshly cleaved crystal in air, where a red line indicates the variation of the wavelength of the emission peak as a function of time. The PL peak is redshifted from 546 to 560 nm in about 25 ns. This behavior is in contrast to what is observed for two-photon excitation, where the emission peak wavelength remains unchanged with time. Similar behavior was recently reported by Yamada et al. (31) for MAPbI$_3$ crystals, where they suggested that the redshift probably originates from the diffusion of photoexcited carriers from the surface to the interior of the crystal. To verify this, we calculated the photocarrier distribution and simulated the PL spectrum at various times after single-photon excitation (see the Supplementary Materials for details). Figure 3E presents the calculated photocarrier density profiles as a function of distance from the crystal surface. Although the carrier density near the surface decreases with time, the bulk carrier density increases because of their long diffusion length. The calculated PL spectrum (Fig. 3F) correctly reproduces the experimental results, confirming that the redshift originates from carrier diffusion.

Low SRV in MAPbBr$_3$ crystals

The time evolution of the carrier density after their generation is governed by their diffusion and recombination. Recombination mechanisms include Shockley-Read-Hall processes, radiative recombination, and Auger recombination, as well as surface and/or interface recombination; all these mechanisms contribute directly or indirectly to the observed PL recombination dynamics. Although there are several different recombination channels, it is possible to classify them into two categories: bulk recombination and surface recombination, as illustrated in Fig. 4A. The effective lifetime of the carriers, which can be obtained from TRPL, is described as the sum of the recombination rates: $1/\tau = 1/\tau_b + 1/\tau_s$, where τ_b is the bulk recombination lifetime and τ_s is the surface recombination lifetime. The bulk recombination lifetime τ_b can be determined from the TRPL measured by two-photon excitation. Our analysis in the previous section suggests that the two-photon excitation corresponds to a low injection regime (the estimated photocarrier density is 1.9×10^{13} cm^{-3}). It is noted that the carrier lifetime is not significantly affected by reabsorption and reemission effect; measurements performed in transmission and reflection geometry give rise to similar results. The bulk recombination rate is estimated to be $1/\tau_b = 2.2 \times 10^{-5}$ s^{-1} using the lifetime of 4.5 μs measured by two-photon excitation. Furthermore, using single-photon excitation (see previous section), the effect of surface states in the single
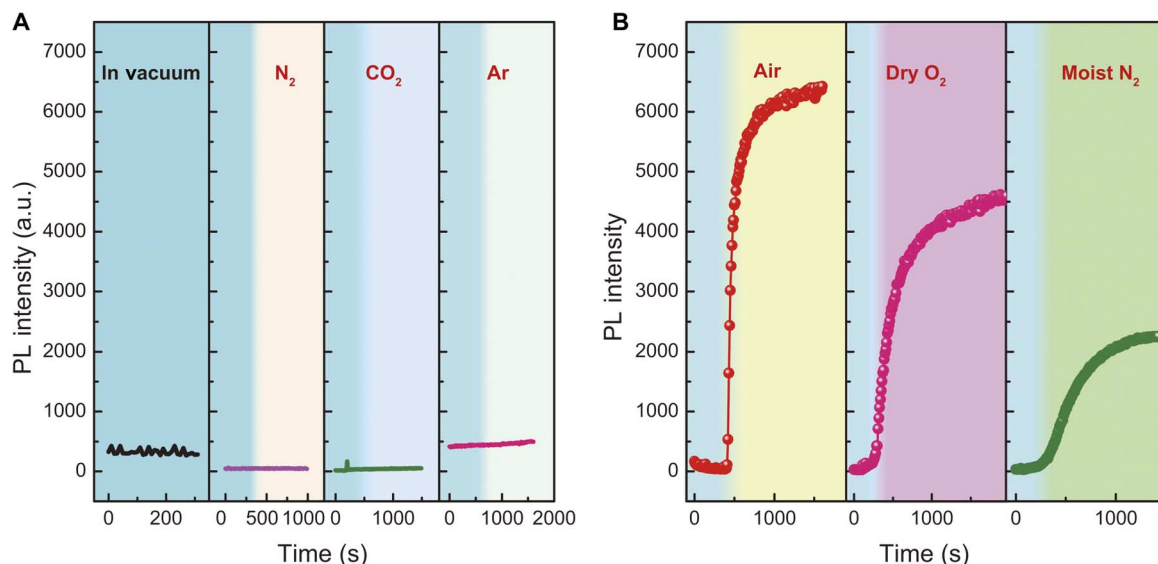
Fig. 2. Effect on the PL intensity of MAPbBr$_3$ single crystals of exposure to different gaseous environments. (**A**) PL intensity as a function of time in vacuum and on exposure to dry N$_2$, dry CO$_2$, and dry Ar. (**B**) PL intensity as a function of time on exposure to air, dry O$_2$, and moist N$_2$. In each panel, the blue shaded area indicates vacuum. The crystal was excited with a 400-nm wavelength laser; the laser power was kept constant at 0.71 μJ/cm^2.
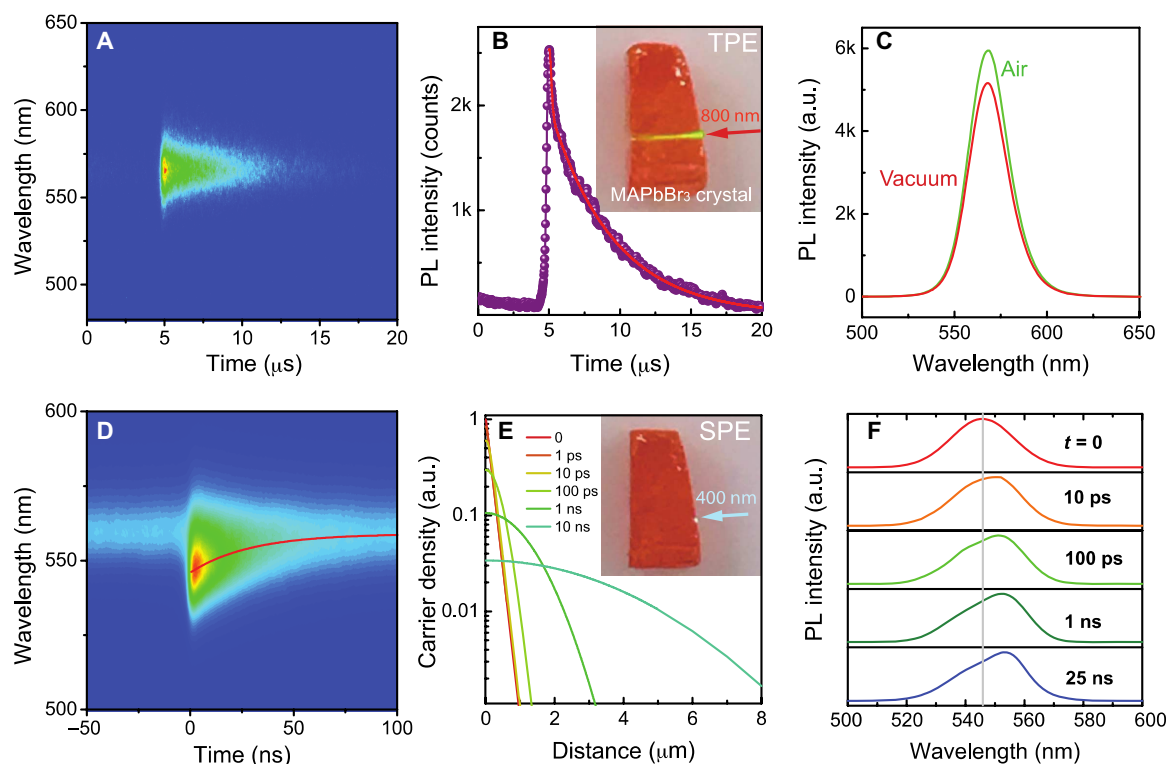

Fig. 3. Two-photon excited fluorescence in MAPbBr$_3$ crystal and single-photon excited optical properties of cleaved crystal surface. (**A**) 2D pseudo-color plot of two-photon (800 nm) excited TRPL measured in air. (**B**) TRPL dynamics [extracted from measurement reported in (A)]; the fit gives lifetimes of $t_1 = 34$ ns and $t_2 = 4.5$ μs. Inset: Image of MAPbBr$_3$ crystal under two-photon excitation (TPE) with an excitation wavelength of 800 nm. (**C**) Two-photon excited PL spectra measured in air and vacuum. (**D**) 2D pseudocolor plot of TRPL of a freshly cleaved crystal in air; the excitation wavelength is 400 nm. The emission peak wavelength as a function of time is indicated by the red line. (**E**) Calculated photocarrier density profile at various times under 400-nm laser excitation. Inset: Image of MAPbBr$_3$ crystal under single-photon excitation (SPE) with an excitation wavelength of 400 nm. (**F**) Calculated PL spectra at various times after excitation.
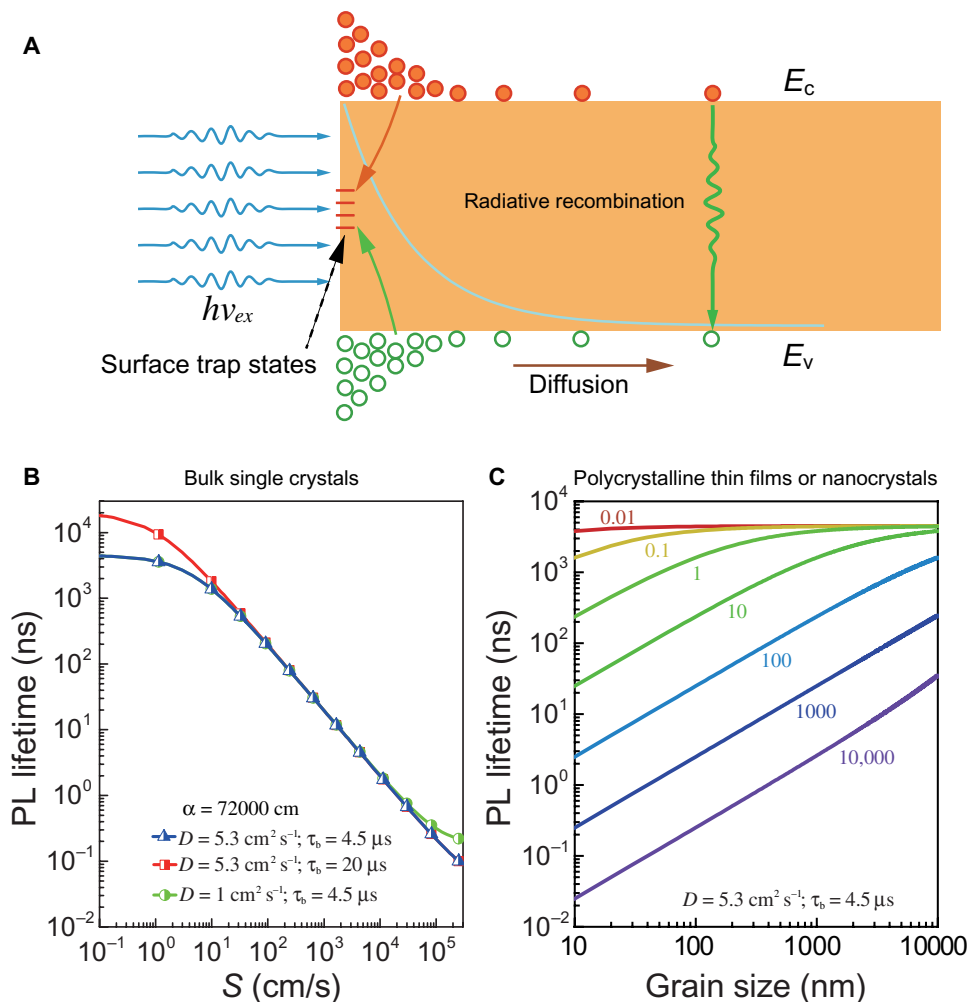
Fig. 4. Effect of surface recombination on the optical properties of MAPbBr$_3$ crystal. (**A**) Schematic image showing photoexcitation and deep levels within the forbidden gap in proximity to the surface. hv_{ex}, excitation laser; E_c, conduction band; E_v, valence band. (**B**) PL lifetime in bulk single crystals as a function of SRV for various carrier diffusion coefficients and bulk lifetimes. (**C**) PL lifetime in polycrystalline thin film or small crystals for various surface recombination velocities.

crystals can be quantified by extracting the SRV (*S*) using the following equation (*32*)

$$\frac{1}{\tau_s} = \frac{2\alpha^2 D}{1 + \sqrt{1 + 8\alpha^2 D^2 / S^2}}$$

where α is the absorption coefficient at the excitation wavelength, and $D = \mu kT/q$ is the carrier diffusion coefficient. This expression is applicable if the sample thickness *d* is much larger than the optical penetration depth α^{-1}, which is the case for the single-photon excitation study on our monocrystals. With the above expression, an SRV (*S*) = 4 cm/s is obtained from crystals with pristine surface, giving $\mu = 206$ cm^2 V^{-1} S^{-1} as measured by the time of flight method (*33*). Also, an effective lifetime of 2.3 μs (see fig. S12) measured at low excitation fluence of 10 nJ/cm^2 is used. The above general expression reduces to $1/\tau_s = \alpha S/\sqrt{2}$ for small *S* values, showing that the result is robust toward variation of the charge carrier mobility. An SRV (*S*) = 2.9 cm/s is obtained if $1/\tau_s = \alpha S$

is used as proposed by Ahrenkiel and Dashdorj (*34*). This is the lowest SRV value ever reported for hybrid perovskites (three orders of magnitude lower than previously reported values) (*35*). It is also much lower than the SRV values for detector grade semiconducting crystals, such as silicon (2×10^4 cm/s) and germanium (1300 cm/s) (*36*). It is noteworthy that the surfaces of these MAPbBr$_3$ crystals are not intentionally passivated.

The SRV can be described using the equation $S = \sigma v_{th} N_t$ (*37*), where $v_{th} \approx 3.7 \times 10^7$ cm/s is the carrier thermal velocity, $\sigma \approx 10^{-15}$ cm^2 is a typical recombination surface cross section in semiconductors, and N_t is the number of recombination centers per square centimeter. Under these assumptions, we deduce the surface density of electronic defects to be less than 10^8 cm^{-2}. As discussed above, the PL lifetime is shortened to be 22 ns when the sample is exposed to vacuum. Under this condition, the calculated SRV in vacuum increases to $S = 890$ cm/s, corresponding to a surface density of defect states of 2.4×10^{10} cm^{-2}, which is two orders of magnitude higher than that in air. The effective PL lifetimes for large crystals are plotted with different carrier diffusion coefficients *D* and bulk lifetimes τ_b in Fig. 4B. We found that the single-photon excitation

PL lifetime in bulk crystals is mainly limited by the SRV and, thus, by the density of surface trap states. When the SRV varies from 1 to 10^4 cm/s, the PL lifetime also varies from microseconds to nanoseconds. This further indicates that MAPbBr$_3$ single crystals may have great potential for detecting oxygen and water vapor.

One of the most attractive features of hybrid perovskites is their ability to form efficient polycrystalline thin films by low-temperature solution processes for cheap mass production of solar cells. Precise knowledge of the surface recombination effect on polycrystalline thin films as well as on colloidal perovskite nanocrystals is therefore of high interest for the improvement of perovskite devices. Here, we made the assumption that surface traps at the thin film grain boundary and/or at the nanocrystal surface are of the same nature as the ones in the single crystals. Given that grain boundaries and the surfaces of each grain have the same concentration of recombination center per unit area, the PL lifetime as a function of the grain size in the film or nanocrystal can be described by the equation (35)

$$\frac{1}{\tau_s} = \frac{1}{\tau_b} + \frac{2}{\frac{d}{S} + \frac{1}{D}\left(\frac{d}{\pi}\right)^2}$$

where d is the size of the grain in the film or nanocrystal, S is the SRV, and D is the carrier diffusion coefficient. This expression is applicable if the sample thickness d is small, such that the carriers can easily diffuse from one surface to the opposite surface, which is the case for single-photon excitation studies on thin films. Figure 4C displays the PL lifetime as a function of grain size at different SRVs. In contrast to bulk crystals, the grain size plays a major role (Fig. 4B and previous equation). For small

grain size d, the effective PL lifetime approaches the bulk recombination lifetime. This occurs only if the surface of the perovskite material is well passivated, so that the surface state density is much lower than that of the bulk defect states. In the case where the thin film has the same bulk recombination lifetime as the monocrystal and the grain size is about 1 μm, the SRV would be less than 1 cm/s, corresponding to a surface density of 3.7×10^7 cm^{-2}.

Electronic properties of single crystals

To directly evaluate how the electronic properties are modulated by the interaction between ambient gas molecules and the defect sites, we proceeded to investigate the charge-transport properties of MAPbBr$_3$ single crystal devices in vacuum and air. For this purpose, we fabricated devices by evaporating Au electrodes (40 nm) on the monocrystals with channel length of 120 μm, as illustrated in Fig. 5. Figure 5D shows the measured current as a function of applied bias with and without laser illumination both in air and in vacuum. At an applied bias of 1.5 V, the current obtained in vacuum is about 40 nA and increases to 50 nA after air exposure. A similar but larger effect is observed in the presence of the laser illumination; the current increases from 10 μA in vacuum to 24 μA in air. The current variation is reversible when the device is re-measured under vacuum. It is important to note that the change in photocurrent is much larger than that of the dark current. The current in the crystal can be expressed as $I = I_b + I_s$, where I_b is the bulk contribution and I_s is the current near the surface. Because of the short penetration depth of the incoming 405-nm light beam, most of the photogenerated carriers are located near the surface rather than in the bulk. We indeed observed that
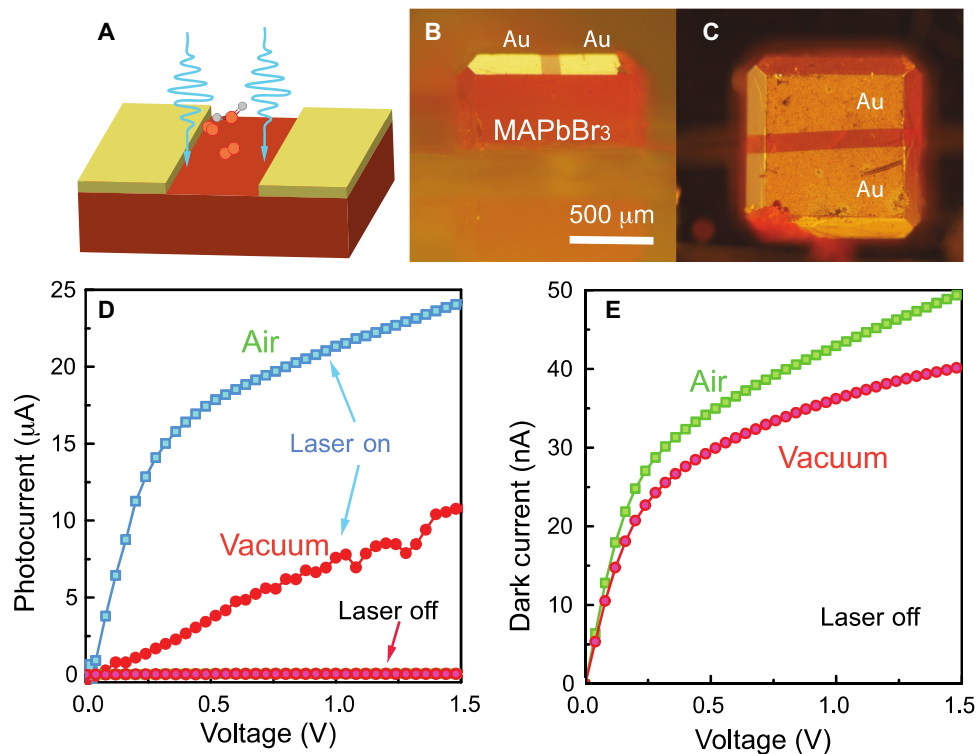

Fig. 5. Electronic properties of MAPbBr$_3$ single-crystal devices. (**A**) Structure of the single-crystal device for current-voltage (*I-V*) measurement. (**B** and **C**) Side-view and top-view of a single-crystal device. (**D**) *I-V* curves of the MAPbBr$_3$ single-crystal device under laser illumination in air and vacuum. (**E**) Dark current of the MAPbBr$_3$ single-crystal device in air and vacuum.

the photocurrent is easily modulated by exposing the crystal surface to air or vacuum, confirming that the surface trap sites play an important role in determining the optoelectronic properties of MAPbBr$_3$ single crystals.

The oxygen and water molecules have been shown to effectively modulate the optoelectronic properties of MAPbBr$_3$ single crystals. Recently, Tian et al. (38) reported that trapping sites in MAPbI$_3$ can be deactivated by a photochemical reaction involving oxygen and causing a nonreversible PL enhancement. It should be emphasized that the interaction between gases and perovskites is strongly dependent on both the chemical nature of the material and the local composition. The PL modulation in MAPbBr$_3$ single crystals is fast and fully reversible; thus, it is reasonable to think that is because of physical processes (physisorptions) rather than photochemical reactions. Meanwhile, the MAPbBr$_3$ crystals show high photostability under ambient conditions (see fig. S3), in contrast to MAPbI$_3$ (39). In a recent study combining experiments and modeling, it has been shown that electrons are trapped by Pb^{2+} cations in MAPbBr$_3$ and related compounds (40). Loss of bromide at the surface of the perovskite leads to vacancy sites and undercoordination of the Pb atom, resulting in a net positive charge at the crystal surface. It then creates favorable conditions for coordination with electron-rich molecules, such as Lewis bases, for example, thiophene (41). Such defects have been observed in low-temperature scanning tunneling microscopy studies of MAPbBr$_3$ crystals (42). Thus, a possible reason for the observed PL modulation effect is that the reversible physisorption of O$_2$ and H$_2$O acts as a type of "molecular gating" that donates electron density to the Pb^{2+} cation. This helps to effectively neutralize the excess positive charges and therefore to drastically modulate the surface recombination rate in MAPbBr$_3$ single crystals.

CONCLUSION

In summary, we have synthesized MAPbBr$_3$ single crystals with an extremely low surface recombination rate. The measured SRV rate is so far the lowest reported in hybrid perovskites. We have observed that the PL properties of the crystals can be drastically modulated by exposing them to different gases. In this way, the surface state density can be controlled, and the process is fully reversible. These results have important implications for the design and fabrication of future devices under different environmental conditions. In particular, the large variation in the PL intensity and lifetime observed in the present study could provide a basis for the application of MAPbBr$_3$ perovskite as gas detectors. Therefore, our results not only shed light on the defect physics of hybrid perovskites but also offer a new route toward tailoring their physical properties by defect engineering.

MATERIALS AND METHODS

Materials

All reagents were purchased from commercial vendors and used as received. Test gases [N$_2$, He, Ar, CO$_2$, and a mixture of O$_2$ (20%) and He (80%)] were obtained from Linde Gas. Other reagents used were lead bromide (PbBr$_2$) (>98%; Sigma-Aldrich), methylamine hydrobromide (>98.0%; Alfa Aesar, TCI), N,N'-dimethylformamide (DMF) (>99.8%; Alfa Aesar), and dichloromethane (DCM) (99.7%; Alfa Aesar).

Growth of MAPbBr$_3$ single crystals

MAPbBr$_3$ single crystals were prepared from solution by ITC or AVC. In the ITC method, PbBr$_2$ and methylamine bromide (MABr) with a molar ratio of 1:1 were dissolved in N,N'-DMF to form a solution, and

CH$_3$NH$_3$PbBr$_3$ was crystallized at 60°C. In the AVC method, PbBr$_2$ and MABr were dissolved in 5-ml DMF solution in a 20-ml vial with a molar ratio of 1:1. The vial was sealed with foil, but left a small hole to let DCM slowly enter. The vial was stored in an atmosphere of DCM, under which conditions MAPbBr$_3$ single crystals slowly grew, reaching a size of a few millimeters after several days.

Optical measurement

PL measurements were performed by exciting the samples with the second harmonic (400 nm) of a mode-locked Ti/sapphire laser (Mira 900, Coherent). The laser power was adjusted using neutral density filters. The excitation beam was spatially limited by an iris and focused with a 150-mm focal length lens. Fluorescence was collected into a spectrometer with a 50 lines/mm grating and recorded with an ImagEM CCD camera from Hamamatsu. The spectra were corrected for the spectral response of the setup. Time-resolved traces were recorded with a Hamamatsu streak camera working in single-sweep mode. The excitation source was the same mode-locked femtosecond laser with a repetition rate of 76 MHz; a pulse picker was inserted on the optical path to decrease the repetition rate of the laser pulses when needed. For the two-photon excited PL measurement, the fundamental laser pulse from the mode-locked Ti/sapphire laser was used, and the power density was adjusted to be 18.5 μJ/cm^2 by neutral density filters.

Charge-transport measurement

Electrical contacts were prepared by depositing gold on the largest natural facet of an MAPbBr$_3$ crystal in a coplanar configuration. We used a gold microwire as a shadow mask before depositing the gold electrodes. A Keithley 2400 SourceMeter was used for electrical characterization. In photoconductivity measurements, the top surface of the crystal was illuminated at normal incidence using a laser diode with a wavelength of 405 nm.

SUPPLEMENTARY MATERIALS

Supplementary material for this article is available at http://advances.sciencemag.org/cgi/content/full/2/7/e1600534/DC1

fig. S1. Powder XRD pattern of crushed MAPbBr$_3$ crystals.
fig. S2. PL excitation spectrum and PL of a MAPbBr$_3$ single crystal measured at room temperature in ambient air.
fig. S3. Photostability of MAPbBr$_3$ single crystal.
fig. S4. PL spectra taken at different vacuum levels.
fig. S5. PL spectra of crystals prepared by the AVC technique in vacuum and air.
fig. S6. Steady-state and TRPL spectrum from a freshly cleaved crystal prepared by the ITC technique in vacuum and air.
fig. S7. TRPL decay in vacuum from a crystal grown by ITC.
fig. S8. PL intensity variation in different gases.
fig. S9. Normalized PL spectra in different gases.
fig. S10. PL intensity as a function of time in air under two-photon excitation (800 nm).
fig. S11. Photocarrier distribution at $t = 0$ under single- and two-photon excitation conditions.
fig. S12. TRPL spectrum from a crystal prepared by the ITC technique under lower power density of 400-nm excitation.
movie S1. Perovskite crystal under excitation of a 400-nm wavelength laser from an atmosphere of air to vacuum and then to air.
References (43–45)

REFERENCES AND NOTES

1. N. J. Jeon, J. H. Noh, W. S. Yang, Y. C. Kim, S. Ryu, J. Seo, S. I. Seok, Compositional engineering of perovskite materials for high-performance solar cells. Nature 517, 476–480 (2015).
2. H. Zhou, Q. Chen, G. Li, S. Luo, T.-b. Song, H.-S. Duan, Z. Hong, J. You, Y. Liu, Y. Yang, Interface engineering of highly efficient perovskite solar cells. Science 345, 542–546 (2014).

3. M. M. Lee, J. Teuscher, T. Miyasaka, T. N. Murakami, H. J. Snaith, Efficient hybrid solar cells based on meso-superstructured organometal halide perovskites. *Science* **338**, 643–647 (2012).

4. M. Liu, M. B. Johnston, H. J. Snaith, Efficient planar heterojunction perovskite solar cells by vapour deposition. *Nature* **501**, 395–398 (2013).

5. Research Cell Efficiency Records (National Renewable Energy Laboratory), available at www.nrel.gov/ncpv/, Rev. 04-20-2016.

6. Z.-K. Tan, R. S. Moghaddam, M. L. Lai, P. Docampo, R. Higler, F. Deschler, M. Price, A. Sadhanala, L. M. Pazos, D. Credgington, F. Hanusch, T. Bein, H. J. Snaith, R. H. Friend, Bright light-emitting diodes based on organometal halide perovskite. *Nat. Nanotechnol.* **9**, 687–692 (2014).

7. G. Xing, N. Mathews, S. S. Lim, N. Yantara, X. Liu, D. Sabba, M. Grätzel, S. Mhaisalkar, T. C. Sum, Low-temperature solution-processed wavelength-tunable perovskites for lasing. *Nat. Mater.* **13**, 476–480 (2014).

8. F. Deschler, M. Price, S. Pathak, L. E. Klintberg, D.-D. Jarausch, R. Higler, S. Hüttner, T. Leijtens, S. D. Stranks, H. J. Snaith, M. Atatüre, R. T. Phillips, R. H. Friend, High photoluminescence efficiency and optically pumped lasing in solution-processed mixed halide perovskite semiconductors. *J. Phys. Chem. Lett.* **5**, 1421–1426 (2014).

9. Y. Fang, Q. Dong, Y. Shao, Y. Yuan, J. Huang, Highly narrowband perovskite single-crystal photodetectors enabled by surface-charge recombination. *Nat. Photonics* **9**, 679–686 (2015).

10. L. Dou, Y. M. Yang, J. You, Z. Hong, W.-H. Chang, G. Li, Y. Yang, Solution-processed hybrid perovskite photodetectors with high detectivity. *Nat. Commun.* **5**, 5404 (2014).

11. H. J. Snaith, Perovskites: The emergence of a new era for low-cost, high-efficiency solar cells. *J. Phys. Chem. Lett.* **4**, 3623–3630 (2013).

12. G. Xing, N. Mathews, S. Sun, S. S. Lim, Y. M. Lam, M. Grätzel, S. Mhaisalkar, T. C. Sum, Long-range balanced electron-and hole-transport lengths in organic-inorganic $CH_3NH_3PbI_3$. *Science* **342**, 344–347 (2013).

13. S. D. Stranks, G. E. Eperon, G. Grancini, C. Menelaou, M. J. P. Alcocer, T. Leijtens, L. M. Herz, A. Petrozza, H. J. Snaith, Electron-hole diffusion lengths exceeding 1 micrometer in an organometal trihalide perovskite absorber. *Science* **342**, 341–344 (2013).

14. H. J. Snaith, A. Abate, J. M. Ball, G. E. Eperon, T. Leijtens, N. K. Noel, S. D. Stranks, J. T.-W. Wang, K. Wojciechowski, W. Zhang, Anomalous hysteresis in perovskite solar cells. *J. Phys. Chem. Lett.* **5**, 1511–1515 (2014).

15. D. W. de Quilettes, S. M. Vorpahl, S. D. Stranks, H. Nagaoka, G. E. Eperon, M. E. Ziffer, H. J. Snaith, D. S. Ginger, Impact of microstructure on local carrier lifetime in perovskite solar cells. *Science* **348**, 683–686 (2015).

16. Y. Shao, Z. Xiao, C. Bi, Y. Yuan, J. Huang, Origin and elimination of photocurrent hysteresis by fullerene passivation in $CH_3NH_3PbI_3$ planar heterojunction solar cells. *Nat. Commun.* **5**, 5784 (2014).

17. X. Wu, M. T. Trinh, D. Niesner, H. Zhu, Z. Norman, J. S. Owen, O. Yaffe, B. J. Kudisch, X.-Y. Zhu, Trap states in lead iodide perovskites. *J. Am. Chem. Soc.* **137**, 2089–2096 (2015).

18. W. Nie, H. Tsai, R. Asadpour, J.-C. Blancon, A. J. Neukirch, G. Gupta, J. J. Crochet, M. Chhowalla, S. Tretiak, M. A. Alam, H.-L. Wang, A. D. Mohite, High-efficiency solution-processed perovskite solar cells with millimeter-scale grains. *Science* **347**, 522–525 (2015).

19. C. Bi, Q. Wang, Y. Shao, Y. Yuan, Z. Xiao, J. Huang, Non-wetting surface-driven high-aspect-ratio crystalline grain growth for efficient hybrid perovskite solar cells. *Nat. Commun.* **6**, 7747 (2015).

20. W. S. Yang, J. H. Noh, N. J. Jeon, Y. C. Kim, S. Ryu, J. Seo, S. I. Seok, High-performance photovoltaic perovskite layers fabricated through intramolecular exchange. *Science* **348**, 1234–1237 (2015).

21. D. Shi, V. Adinolfi, R. Comin, M. Yuan, E. Alarousu, A. Buin, Y. Chen, S. Hoogland, A. Rothenberger, K. Katsiev, Y. Losovyj, X. Zhang, P. A. Dowben, O. F. Mohammed, E. H. Sargent, O. M. Bakr, Low trap-state density and long carrier diffusion in organolead trihalide perovskite single crystals. *Science* **347**, 519–522 (2015).

22. M. I. Saidaminov, A. L. Abdelhady, B. Murali, E. Alarousu, V. M. Burlakov, W. Peng, I. Dursun, L. Wang, Y. He, G. Maculan, A. Goriely, T. Wu, O. F. Mohammed, O. M. Bakr, High-quality bulk hybrid perovskite single crystals within minutes by inverse temperature crystallization. *Nat. Commun.* **6**, 7586 (2015).

23. G. E. Eperon, S. N. Habisreutinger, T. Leijtens, B. J. Bruijnaers, J. J. van Franeker, D. W. deQuilettes, S. Pathak, R. J. Sutton, G. Grancini, D. S. Ginger, R. A. J. Janssen, A. Petrozza, H. J. Snaith, The importance of moisture in hybrid lead halide perovskite thin film fabrication. *ACS Nano* **9**, 9380–9393 (2015).

24. S. Pathak, A. Sepe, A. Sadhanala, F. Deschler, A. Haghighirad, N. Sakai, K. C. Goedel, S. D. Stranks, N. Noel, M. Price, S. Hüttner, N. A. Hawkins, R. H. Friend, U. Steiner, H. J. Snaith, Atmospheric influence upon crystallization and electronic disorder and its impact on the photophysical properties of organic–inorganic perovskite solar cells. *ACS Nano* **9**, 2311–2320 (2015).

25. Y. Tian, A. Merdasa, E. Unger, M. Abdellah, K. Zheng, S. McKibbin, A. Mikkelsen, T. Pullerits, A. Yartsev, V. Sundström, I. G. Scheblykin, Enhanced organo-metal halide perovskite photo-luminescence from nanosized defect-free crystallites and emitting sites. *J. Phys. Chem. Lett.* **6**, 4171–4177 (2015).

26. C. Müller, T. Glaser, M. Plogmeyer, M. Sendner, S. Döring, A. A. Bakulin, C. Brzuska, R. Scheer, M. S. Pshenichnikov, W. Kowalsky, A. Pucci, R. Lovrinčić, Water infiltration in methylammonium lead iodide perovskite: Fast and inconspicuous. *Chem. Mater.* **27**, 7835–7841 (2015).

27. G. Grancini, V. D'Innocenzo, E. R. Dohner, N. Martino, A. R. S. Kandada, E. Mosconi, F. De Angelis, H. I. Karunadasa, E. T. Hoke, A. Petrozza, $CH_3NH_3PbI_3$ perovskite single crystals: Surface photophysics and their interaction with the environment. *Chem. Sci.* **6**, 7305–7310 (2015).

28. F. Zheng, L. Z. Tan, S. Liu, A. M. Rappe, Rashba spin–orbit coupling enhanced carrier lifetime in $CH_3NH_3PbI_3$. *Nano Lett.* **15**, 7794–7800 (2015).

29. D. Kuciauskas, A. Kanevce, J. M. Burst, J. N. Duenow, R. Dhere, D. S. Albin, D. H. Levi, R. K. Ahrenkiel, Minority carrier lifetime analysis in the bulk of thin-film absorbers using subbandgap (two-photon) excitation. *IEEE J. Photovolt.* **3**, 1319–1324 (2013).

30. R. Sheng, A. Ho-Baillie, S. Huang, S. Chen, X. Wen, X. Hao, M. A. Green, Methylammonium lead bromide perovskite-based solar cells by vapor-assisted deposition. *J. Phys. Chem. C* **119**, 3545–3549 (2015).

31. Y. Yamada, T. Yamada, L. Q. Phuong, N. Maruyama, H. Nishimura, A. Wakamiya, Y. Murata, Y. Kanemitsu, Dynamic optical properties of $CH_3NH_3PbI_3$ single crystals as revealed by one- and two-photon excited photoluminescence measurements. *J. Am. Chem. Soc.* **137**, 10456–10459 (2015).

32. H. Wang, K. S. Wong, B. A. Foreman, Z. Y. Yang, G. K. L. Wong, One- and two-photon-excited time-resolved photoluminescence investigations of bulk and surface recombination dynamics in ZnSe. *J. Appl. Phys.* **83**, 4773–4776 (1998).

33. H. Wei, Y. Fang, P. Mulligan, W. Chuirazzi, H.-H. Fang, C. Wang, B. R. Ecker, Y. Gao, M. A. Loi, J. Huang, Sensitive x-ray detectors made of methylammonium-lead tribromide perovskite single crystals. *Nat. Photonics* **10**, 333–339 (2016).

34. R. K. Ahrenkiel, J. Dashdorj, Interface recombination velocity measurement by a contactless microwave technique. *J. Vac. Sci. Technol. B* **22**, 2063–2067 (2004).

35. Y. Yang, Y. Yan, M. Yang, S. Choi, K. Zhu, J. M. Luther, M. C. Beard, Low surface recombination velocity in solution-grown $CH_3NH_3PbBr_3$ single crystal. *Nat. Commun.* **6**, 7961 (2015).

36. N. Derhacobian, P. Fine, J. T. Walton, Y. K. Wong, C. S. Rossington, P. N. Luke, Determination of surface recombination velocity and bulk lifetime in detector grade silicon and germanium crystals. *IEEE Trans. Nucl. Sci.* **41**, 1026–1030 (1994).

37. S. M. Sze, K. K. Ng, *Physics of Semiconductor Devices* (John Wiley & Sons, New Jersey, 2006) pp. 134–196.

38. Y. Tian, M. Peter, E. Unger, M. Abdellah, K. Zheng, T. Pullerits, A. Yartsev, V. Sundström, I. G. Scheblykin, Mechanistic insights into perovskite photoluminescence enhancement: Light curing with oxygen can boost yield thousandfold. *Phys. Chem. Chem. Phys.* **17**, 24978–24987 (2015).

39. J. F. Galisteo-López, M. Anaya, M. E. Calvo, H. Míguez, Environmental effects on the photophysics of organic–inorganic halide perovskites. *J. Phys. Chem. Lett.* **6**, 2200–2205 (2015).

40. I. A. Shkrob, T. W. Marin, Charge trapping in photovoltaically active perovskites and related halogenoplumbate compounds. *J. Phys. Chem. Lett.* **5**, 1066–1071 (2014).

41. N. K. Noel, A. Abate, S. D. Stranks, E. S. Parrott, V. M. Burlakov, A. Goriely, H. J. Snaith, Enhanced photoluminescence and solar cell performance via Lewis base passivation of organic–inorganic lead halide perovskites. *ACS Nano* **8**, 9815–9821 (2014).

42. R. Ohmann, L. K. Ono, H.-S. Kim, H. Lin, M. V. Lee, Y. Li, N.-G. Park, Y. Qi, Real-space imaging of the atomic structure of organic–inorganic perovskite. *J. Am. Chem. Soc.* **137**, 16049–1654 (2015)

43. H.-H. Fang, J. Yang, J. Feng, T. Yamao, S. Hotta, H.-B. Sun, Functional organic single crystals for solid-state laser applications. *Laser Photonics Rev.* **8**, 687–715 (2014).

44. G. Walters, B. R. Sutherland, S. Hoogland, D. Shi, R. Comin, D. P. Sellan, O. M. Bakr, E. H. Sargent, Two-photon absorption in organometallic bromide perovskites. *ACS Nano* **9**, 9340–9346 (2015).

45. J. Vaitkus, The nonequilibrium hall effect and related transport phenomena in semiconductors under inhomogeneous excitation by a laser pulse. *Phys. Status Solidi A* **34**, 769–775 (1976).

Fang *et al. Sci. Adv.* 2016;2:e1600534   27 July 2016

9 of 9